



Palacios, P. B., Kendall, J. M., & Mader, H. M. (2015). Site effect determination using seismic noise from Tungurahua volcano (Ecuador): implications for seismo-acoustic analysis. *Geophysical Journal International*, 201(2), 1084-1100. DOI: 10.1093/gji/ggv071

Publisher's PDF, also known as Version of record

Link to published version (if available):
[10.1093/gji/ggv071](https://doi.org/10.1093/gji/ggv071)

[Link to publication record in Explore Bristol Research](#)
PDF-document

This is the final published version of the article (version of record). It first appeared online via Oxford University Press at <http://gji.oxfordjournals.org/content/201/2/1084.full>.

University of Bristol - Explore Bristol Research

General rights

This document is made available in accordance with publisher policies. Please cite only the published version using the reference above. Full terms of use are available:
<http://www.bristol.ac.uk/pure/about/ebr-terms.html>

Site effect determination using seismic noise from Tungurahua volcano (Ecuador): implications for seismo-acoustic analysis

Pablo Palacios,^{1,2} J-Michael Kendall¹ and Heidy Mader¹

¹*School of Earth Sciences, University of Bristol, Bristol, UK. E-mail: pablo.palacios@bristol.ac.uk*

²*Geophysical Institute of National Polytechnic School, Quito, Ecuador*

Accepted 2015 February 11. Received 2015 January 26; in original form 2014 August 16

SUMMARY

Scattering and refractions that occur in the heterogeneous near-surface beneath seismic stations can strongly affect the relative amplitudes recorded by three-component seismometers. Using data from Tungurahua volcano we have developed a procedure to correct these ‘site effects’. We show that seismic noise signals store site information, and then use their normalized spectral amplitudes as site frequency response functions. The process does not require a reference station (as per the *S*-wave and coda methods) or assume that the vertical amplitude is constant (the *H/V* component ratio method). Correcting the site effects has three consequences on data analysis: (1) improvement of the seismic source location and its energy estimation; (2) identification of a strong influence on the volcanic acoustic seismic ratio (VASR) and (3) decoupling the air wave impact on the ground caused by explosions or eruption jets. We show how site effect corrections improve the analysis of an eruption jet on 2006 July 14–15, appearing two periods of strong acoustic energy release and a progressive increase of the seismic energy, reaching the maximum before finishing the eruption.

Key words: Site effects; Volcano seismology; Acoustic properties; Explosive volcanism.

1 INTRODUCTION

Seismic waves have a spectral signature that depends on the source mechanism modified by the medium (the path) and by local layers and heterogeneities beneath the stations that record the signals. This last transformation, due to refractions and scatterings, is known as the ‘site effect’ (e.g. Sato *et al.* 2012). The Michoacán earthquake in Mexico, on 1985 September 19, produced large seismic intensities and severe damage in Mexico City. The site effect influence is one of the key factors needed to explain this disaster (Campillo *et al.* 1989). Determining the site effect is useful in a number of ways, including hazard assessment and the determination of source properties.

Aki (1969) and Aki & Chouet (1975) interpreted the site effect as a backscattering process that can be observed and measured using coda waves, which are those portions of seismic signals still oscillating above the noise level and recorded long after the arrival of the leading body waves. Kato *et al.* (1995) applied these concepts, computing the site effect relative to a reference station and compared the results with a method that inverts source and site parameters from *S*-waves spectra (Andrews 1986; Hartzell 1992). Applying the coda-wave method, Kumagai *et al.* (2010) computed the site effect factors for a seismic network on Tungurahua volcano. However, this approach requires good recordings of many local (roughly within 100–300 km.) earthquakes from a broad range of azimuths, which is not always possible.

An alternative is to use seismic noise information to determine the site effect properties. Natural seismic noise is not completely random (i.e. not white noise). It shows a power spectrum that depends on external sources and the site properties (e.g. Peterson 1993), whereas the power spectrum of white noise is expected to be flat because all frequencies have a similar probability of occurrence (e.g. Buttkus 2000). Applications using noise information include tomography studies (e.g. Shapiro *et al.* 2005; Ritzwoller *et al.* 2011; Ward *et al.* 2013), detection of stress changes in fault zones (Wegler & Schönfelder 2007), and volcano monitoring (Clarke *et al.* 2013) (see Prieto *et al.* 2011, for other applications). Such noise has been used to compute the site effects in Arenal (Mora *et al.* 2001) and Vesuvius (Nardone & Maresca 2011) volcanoes, with the *H/V* method proposed by Nakamura (1989) which interprets the spectral ratios of horizontal to vertical components as amplitudes of the frequency response functions (FRF) of layered media. In this method it is assumed that the vertical component amplitude does not change significantly due to site effects compared with those for the horizontal components.

If the signal of a seismic event is given and the site FRF (amplitude and phase) are known, it is possible to remove the site effect by filtering it with the inverse FRF; that is by performing a deconvolution (Buttkus 2000). For methods that use a reference station, the physical interpretation of this deconvolution is equivalent to substituting the local heterogeneities, scatters, layers or other properties

beneath each network station, with those from the reference station. In a similar way, to deconvolve a signal using the H/V method is equivalent to transforming the horizontal properties in order to make them as similar as possible to the vertical. However, the volcano geologic structure is usually stratified; the deposits form layers whose horizontal dimensions are larger than the vertical, leading to significant frequency dependent differences in vertical versus horizontal amplitudes. In addition, because there is usually a significant reduction in wave velocities to some hundreds metres per second, at a few hundreds metres beneath the stations (e.g. Drosos *et al.* 2012), all components of an incoming wave should have amplitude changes. To overcome these restrictions, we introduce an approach that computes the FRF using seismic noise information under the condition that for distant earthquakes, the deconvolved signals at all stations must be similar. This implicitly assumes that the source–receiver path is the same to each station, which is the case if the distance between stations is much smaller than their distance from the source.

Removing the site effects should improve the characterization of the seismic source. This is potentially important for seismo-acoustic studies of volcanic explosions, in which the differences in ratios of acoustic and seismic energies are explained as physical changes related to the source conditions (Hagerty *et al.* 2000; Rowe *et al.* 2000; Johnson *et al.* 2003). Johnson & Aster (2005), Sciotto *et al.* (2011) and Andronico *et al.* (2013) have all noted that the computation of the seismic energy needs to take into account the site effects, which should improve the accuracy of the estimation of the volcanic acoustic seismic ratio (VASR). Additionally, it is frequently observed in the case of volcanic explosions that the air waves are coupled into the seismic record (e.g. Hagerty *et al.* 2000; De Angelis *et al.* 2012). More recently, Ichihara *et al.* (2012) proposed a method based on the cross-correlation of seismic and acoustic signals, to identify the coupling. Matoza & Fee (2014) extended this method to frequency domain using the coherence and applied it to study eruptions of Mount St Helens, Redoubt and Tungurahua volcanoes. Using our approach, removing the site effects improves the procedure of decoupling the acoustic signals mixed within the seismic record, yielding a better estimation of the seismic source energy.

The aim of this paper is to introduce a seismic noise-based frequency-dependent estimate of site effects, without *a priori* assumptions about component amplitudes. We evaluate site effects on three stations on Tungurahua volcano, Ecuador, deployed shortly before two large eruptions in 2006. The seismic and acoustic records of several explosions and an eruption jet on 2006 July 14–15 are analysed.

2 TUNGURAHUA

Tungurahua is an andesitic volcano located on the Eastern Cordillera of the Ecuadorian Andes (long: 78.45W, lat: 1.47S). On 2006 July 14–15 and August 16–17, two eruptions (VEI 2 and 3, respectively) with significant pyroclastic flows were generated (Kumagai *et al.* 2007; Hall *et al.* 2013). Three stations with broad-band seismic and acoustic sensors were installed just a few days (BRUN and BMAS1, Fig. 1) and even hours (BCUS) before the 14 July eruption. The transmission systems and the acoustic sensors of BCUS and BMAS1 stations were destroyed by the impact of pyroclastic flows on 17 August, however the seismic recording continued for several hours.

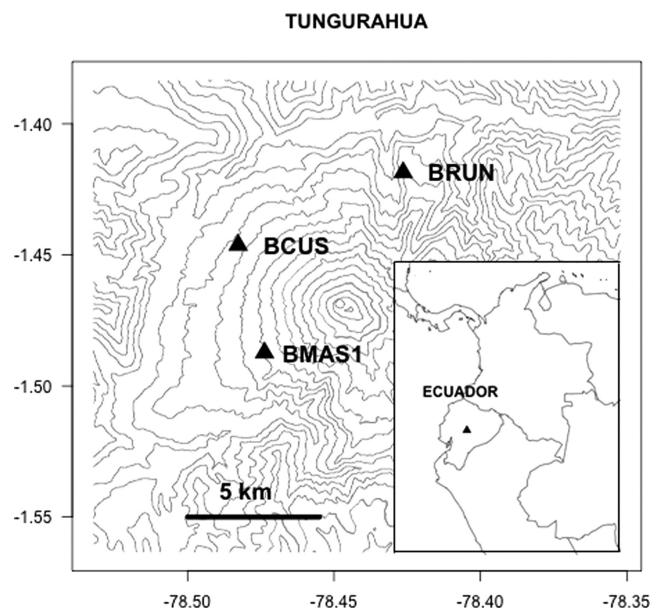


Figure 1. Tungurahua volcano – Ecuador. Stations (BRUN, BCUS and BMAS1) that recorded the eruptions in July and August 2006.

Each network station, BRUN, BCUS and BMAS1, includes a Guralp CMG-40T (0.02–60 s) broad-band seismic sensor and a ACO TYPE 7144/4144 (0.01–10 s) acoustic sensor. The signals are digitized at a 50 Hz sample rate by a Geotech Smart 24D data logger. The digitization process uses filters giving a flat response up to 40 per cent of the sample rate, which limits the flat ranges for the seismic and acoustic signals to 0.02–20 and 0.1–20 Hz, respectively. The seismic sensor is buried at 1–2 m depth and the acoustic sensor is attached to the transmission tower at 1.5 m above the soil. To reduce wind noise, each acoustic sensor is within a metallic cylinder, open at bottom, and protected with an internal foam windscreen. The seismic and acoustic instrumental responses were removed for all data used in this study.

During July and August 2006, Tungurahua volcano was highly active, generating a significant number of explosions and tremors. However, there were some time periods of relative calm that allowed us to identify low activity waveforms considered to be at the noise level. From BCUS and BMAS1 stations, 6.18 hr of noise were collected, while from BRUN a sample of 20 hr of noise was selected (Appendix).

Five earthquakes (Table 1) were chosen to calibrate the site FRF and to evaluate the results. They occurred in a region roughly 50–280 km around Tungurahua ($-4 < \text{lat} < 1$ and $-81 < \text{long} < -76$), and have magnitudes greater than 3.5, with clear arrivals recorded by all three stations. Their entire signals are used in our study, starting five seconds before the arrivals and finishing a number of seconds specified by coda in Table 1. Their locations and magnitudes were computed by Geophysical Institute of National Polytechnic School (IGEPN) and are part of the Earthquake Catalog of Ecuador (Beauval *et al.* 2013).

A sample of twenty explosions that occurred on 2006 July 20–21 (Appendix), were selected to explore their seismic source locations and VASR, before and after removing the site effects. We also explore the seismo-acoustic coupling of the eruption jet on 2006 July 14–15, an event that lasted roughly 4.3 hr.

Table 1. Distant earthquakes around Tungurahua volcano.

| Name | Date | Origin time | Latitude (°) | Longitude (°) | Depth (km) | Distance ^a (km) | Azimuth ^a (°) | Mag | Coda (s) |
|------|----------|-------------|-----------------|------------------|---------------|-------------------------------|-----------------------------|--------|-------------|
| EQ1 | 20060728 | 07:18:45.30 | 0.683 | -76.985 | 3.3 | 284.2 | 215.2 | 4.0 Md | 160 |
| EQ2 | 20060805 | 10:21:20.70 | -2.693 | -78.150 | 12.0 | 143.1 | 345.9 | 3.7 Md | 80 |
| EQ3 | 20060806 | 05:33:02.98 | -3.068 | -80.318 | 51.1 | 278.9 | 48.9 | 4.6 mb | 160 |
| EQ4 | 20060809 | 13:54:10.53 | -1.753 | -80.392 | 12.0 | 217.7 | 81.1 | 4.0 Md | 90 |
| EQ5 | 20060816 | 05:16:20.40 | -1.721 | -78.122 | 12.0 | 50.6 | 308.6 | 4.3 mb | 70 |

^aDistance (hypocentral) and azimuth are average values relative to the stations.

3 SITE EFFECTS

3.1 Background seismic noise

Seismic noise is characterized by a continuous record which is permanently observed over time. Its sources can be cultural or natural. In general, cultural sources are related to high frequencies showing daily, weekly or seasonal periodicities. Peterson (1993) collected noise spectra from a variety of stations spread around the world and showed that they are bounded by a minimum and a maximum spectral models. Thus, the larger amplitudes are detected at very low frequencies with peaks close to semi-diurnal and diurnal periods, and an additional peak is observed in the microseismic band (1–20 s) getting the maximum between 2 and 10 s (0.1–0.5 Hz). Finally, the spectra over 1 Hz are highly variable and likely related to the site response and the presence of cultural activity. Therefore, it is needed to analyse the noise records to identify if their spectra are explained or not by common sources.

The seismic noise signals at Tungurahua's stations have been selected without cultural sources, choosing in time domain those traces that are as uniform as possible and with minimum amplitude during quiescent periods. High frequency content, that is characteristic in cultural or some local sources, is minimum as it is shown in Fig. 5. To explore if there exist effects of common natural sources, we computed the coherence (e.g. Shumway & Stoffer 2010), which is a cross-correlation measure between two signals as a function of their frequency content, for an hour noise sample (on 2006–07–20, merging 02:00–02:40, 17:00–17:17 and 17:19–17:39 periods). The left-hand panels in Fig. 2 show amplitudes of square coherence measures of 60 s windows (which cover the range frequency of Tungurahua's stations), for the vertical components of each station pair. A 10 per cent taper and two 5-length modified-Daniell kernels were used as coherence smoothers. The bottom panel is derived from a simulated station pair with normal and independent white noise records. To discover trends we stacked all coherence amplitude curves and computed their average, shown on the right panels of Fig. 2. The highest mean coherences are observed in the range 0.08–0.4 Hz which is within the microseismic range and likely includes common natural sources and site effects. However, over 0.4 Hz the coherence values are comparable to white noise sources. Similar results are obtained for horizontal components. In all cases the coherence phases do not show relevant information being comparable to white noise sources. Because of this restriction the signals studied in the Section 4 are filtered in the range 0.4–20 Hz.

For further analyses we assume that the seismic noise content, over 0.4 Hz, for the three stations on Tungurahua volcano, are independent. Their spectral properties, like the component ratios, can not be explained by non random common sources. In the next section we explore the differences between the stations on these ratios, in order to find evidences of site effects.

3.2 Spectral ratios of seismic noise and earthquakes

Amplitude spectra, normalized with their area, of seismic noise and five earthquakes are shown in Fig. 3. The major differences at all stations and components are observed below 0.5 Hz, where the microseismicity is dominant. At high frequencies, over 10 Hz, the relative content of energy of earthquakes tend to be less than the noise, likely due to the intrinsic attenuation observed in distant earthquake records. For intermediate frequencies the median spectral shape of noise and earthquakes are closer.

Theoretical and empirical observations support the hypothesis that the spectral ratios of components are related to site response (e.g. Nakamura 1989; Field & Jacob 1993). The amplitude of the spectral ratios of components (north/vertical, east/vertical and east/north) for each of Tungurahua's stations are shown in Fig. 4. They were computed by merging the noise signals into one trace and then cutting it into 300 s segments. Each segment was filtered in the range 0.02–20 Hz with a Butterworth (order 4) filter. The power spectrum density of each segment and component was smoothed summing their values in 0.1 Hz width intervals (value that preserves its dominant shape, saves computing time and minimize ratio outliers), and their square root values were used as spectral amplitudes. Finally, the grey regions show the 95 per cent variation intervals of noise data (spanning 0.025–0.975 quantile of the amplitude ratios), while the black lines are the ratio medians. The median is used as central measure, instead of the mean, to avoid outliers (Leys *et al.* 2013).

It is apparent that each of Tungurahua's station has its own signature and in general, the horizontal components are larger than the vertical. The differences between stations could be caused by external, but local sources, such as rivers, wind or other, and not necessarily by internal scatter excitations or refraction amplifications beneath each station. To address this, a comparison of noise ratios with those from regional but distant earthquakes, helps to decide whether the spectral signatures are dominated or not by external local sources.

Although the earthquakes have larger amplitudes than the noise traces, the median of their component ratios (red lines in Fig. 4) show a similar pattern to the median of the noise, in both shape and size. Mean and median are useful measures to uncover signal trends that drive the global shape of some property, in this case applied to the spectral ratio. Due to the earthquake distances, the spectral signature differences of noise between the stations can not be attributed to external local sources. Such station differences exist in the spectra of Fig. 3, however it is easier to observe them by their ratios, as shown in Fig. 4. This evidence supports the hypothesis that such spectral signatures are dominated by site effects.

Table 2 describes the correlation coefficients, in the frequency domain, between earthquakes ratios and median noise ratios. Better correlations are obtained at BMAS1 and BRUN stations for

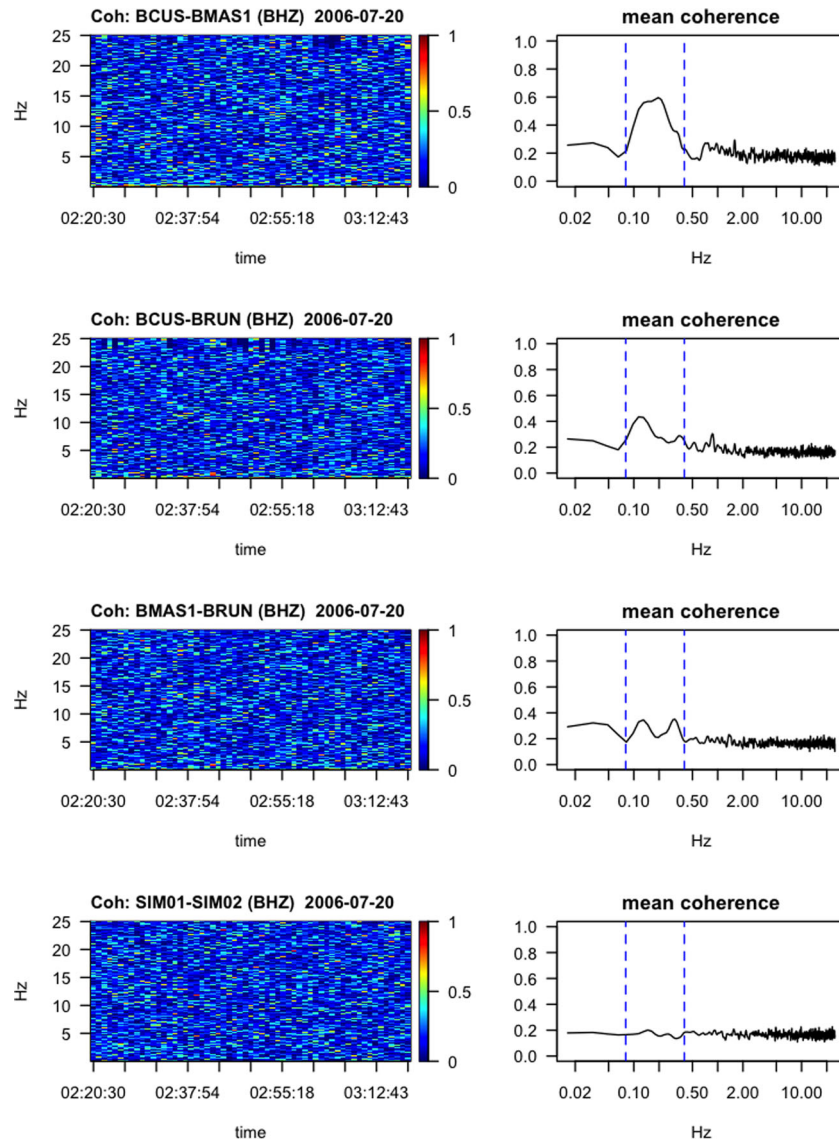


Figure 2. Coherence amplitude of seismic noise. Left-hand panels show it as function of time with 60 s windows, for each station pair. Each right-hand panel is the mean coherence after stacking all windows, as a function of frequency. Vertical dashed lines limit the range 0.08–0.4 Hz. Bottom panels are results from random data.

horizontal to vertical component ratios. These correlation values improve if only frequencies less than 7 Hz are taken into account.

Internal weak volcanic sources will not appear as discrete events because of their low signal-to-noise ratio. However, they may be amplified by layered media, arriving at the stations with a spectral signature that depends on the local geological structure, and actually contributing and forming the recorded noise. The results of Section 3.1 suggest that those sources could be considered as white, independent and randomly distributed (e.g. Sato *et al.* 2012), being valid only over 0.4 Hz. We assume that the noise at the three stations on Tungurahua volcano is formed in this way, therefore containing site information, which is quantified by their corresponding FRF. Nevertheless, it is possible that external local sources also contribute to the noise signals. For example, at frequencies higher than 14 Hz in BCUS station, appears to be that the earthquake ratios are smaller than the noise one, suggesting a high frequency external source. Analysis of such external sources lies outside the scope of this paper.

3.3 Site FRF

Fig. 5 shows the amplitude median functions of each noise component, which needs to be normalized to be used as the site FRF. Each horizontal red line is an arbitrary reference level that could be chosen to differentiate amplifications and attenuations with values greater or less than one, respectively (right vertical axes). No significant phase changes are observed in the median phase functions, therefore, a phase of zero is assumed for them. An earthquake is used to calibrate, or fix each component reference level, such that, after removing the site effect for each station, each component should appear as similar as possible between the stations. The optimal solution is computed as the minimum of an error function, constructed in the spectral domain, that depends on the absolute differences of the earthquake recorded energies (intensities).

After choosing an earthquake the calibration proceeds as follows (Fig. 6). A 5 Hz length window, in frequency domain, is selected as an evaluation range (region between dashed vertical lines in Fig. 5). The reference levels of the noise functions are computed

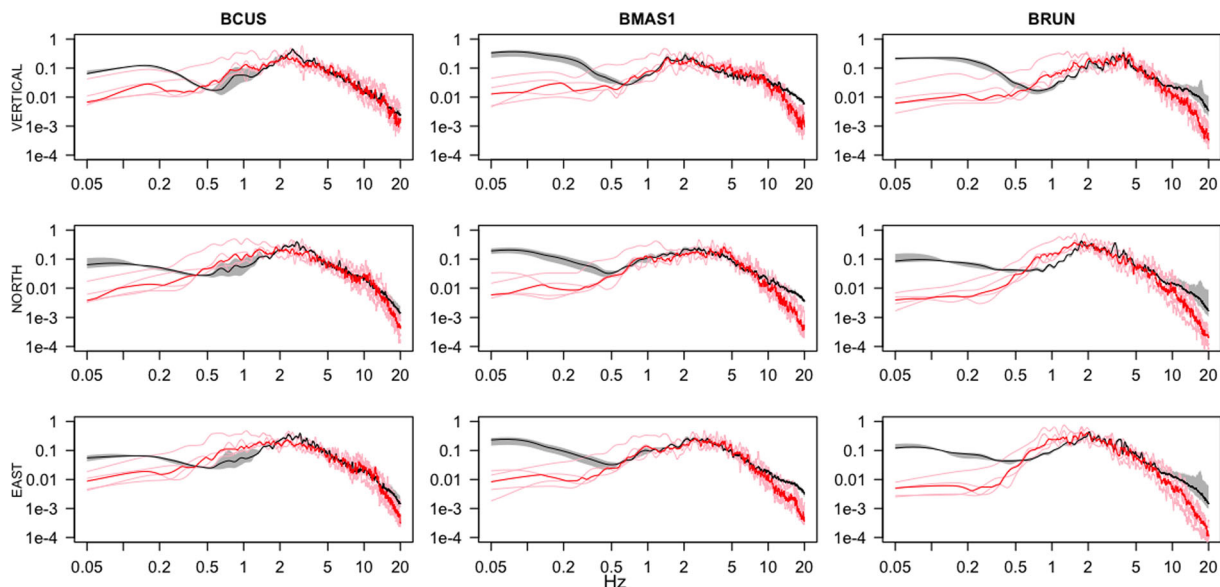


Figure 3. Normalized amplitude spectra of each component at three Tungurahua's stations. Grey regions and black solid lines show 95 per cent intervals and medians of seismic noise spectra, respectively. Pink and red solid lines show spectra and their median, respectively, from five distant earthquakes (EQ1–EQ5).

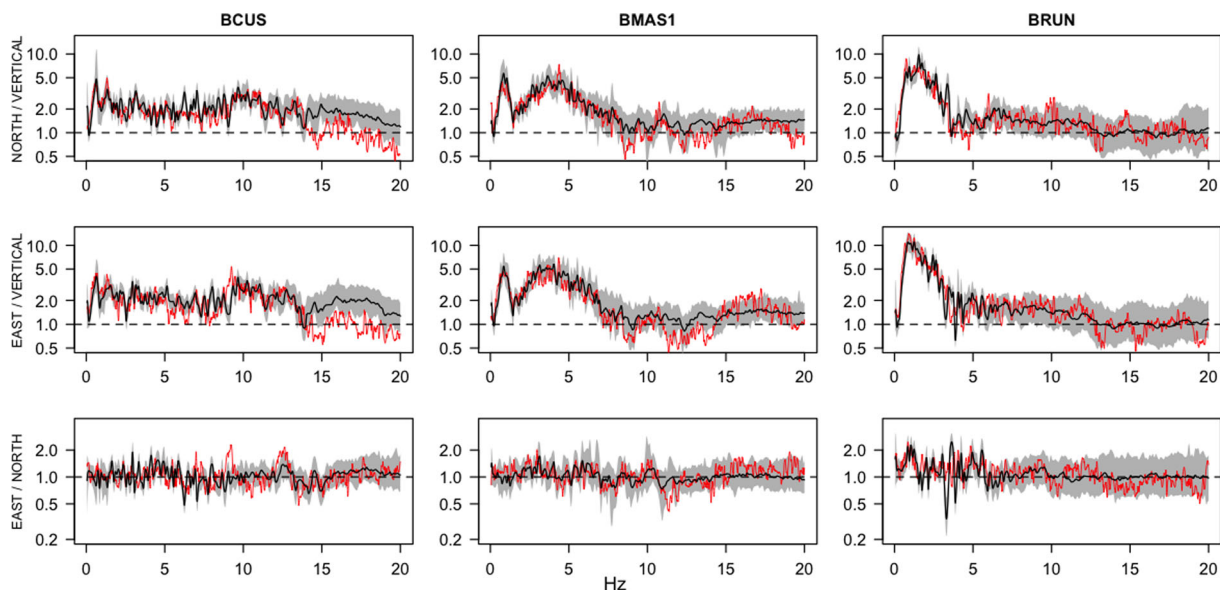


Figure 4. Spectral amplitude ratios at three Tungurahua stations. Grey regions and black solid lines show 95 per cent intervals and medians of noise data, respectively. Red solid lines show medians of amplitude ratios from five distant earthquakes (EQ1–EQ5).

as the mean value of the amplitudes within these ranges. Then, at each station, each vertical, north and east earthquake component is filtered in the range 0.4–20 Hz (due to the restriction of the Section 3.1) and is deconvolved, multiplying it by the inverse FRF of the corresponding component. The deconvolution uses an interpolated function constructed from 0.1 Hz accumulated noise. Then, the coordinate system is rotated, around the vertical axis by an angle equal to the azimuth. Additionally, to take into account the elastic attenuation, the amplitudes of vertical (Z), radial (R) and transversal (T) components are corrected by reducing them to the mean hypocentral distance (Table 1). Namely, if A is the amplitude of one of these component at the station i , d_i the hypocentral distance, and \bar{d} the mean hypocentral distance, the corrected amplitude becomes Ad_i/\bar{d} . We call *reduced energies* those recorded energies computed

with these corrected amplitudes. Finally, the error is computed (see below) and the whole procedure is repeated for a new evaluation range. The 5 Hz evaluation window is moved by 0.3 Hz steps from 0–5 to 15–20 Hz.

In order to compute the errors, the recorded energies are accumulated every 0.1 Hz. If k is an earthquake component (Z, R or T), the error between the stations i and j is defined as

$$\epsilon(i, j|k) = \frac{\sum_f |E_{i|k}(f) - E_{j|k}(f)|}{\sum_f E_{i|k}(f) + \sum_f E_{j|k}(f)}, \quad (1)$$

where $E_{i|k}(f)$ and $E_{j|k}(f)$ are the reduced energies as function of frequency. This function is normalized. Its minimum, zero, is reached only when both power spectra are exactly equal, and its maximum,

Table 2. Correlation in frequency domain of noise versus earthquake ratios.

| Station | Ratio | EQ1 | EQ2 | EQ3 | EQ4 | EQ5 |
|---------|-------|------|------|------|------|------|
| BCUS | N/V | 0.62 | 0.53 | 0.57 | 0.47 | 0.54 |
| | E/V | 0.51 | 0.36 | 0.52 | 0.57 | 0.40 |
| | E/N | 0.22 | 0.03 | 0.17 | 0.18 | 0.04 |
| BMAS1 | N/V | 0.81 | 0.71 | 0.76 | 0.75 | 0.75 |
| | E/V | 0.85 | 0.70 | 0.81 | 0.71 | 0.70 |
| | E/N | 0.33 | 0.26 | 0.30 | 0.35 | 0.22 |
| BRUN | N/V | 0.86 | 0.80 | 0.77 | 0.82 | 0.74 |
| | E/V | 0.86 | 0.87 | 0.91 | 0.91 | 0.84 |
| | E/N | 0.15 | 0.36 | 0.37 | 0.16 | 0.22 |

one, is obtained if one of them is exactly zero at all frequencies. The error of the k component for N stations is defined as

$$\xi_k = \frac{2}{N(N-1)} \sum_{i>j} \epsilon(i, j|k), \quad (2)$$

where the sum runs over all station pairs and is averaged with the number of them, $N(N-1)/2$. This error is normalized, $0 \leq \xi_k \leq 1$. Eventually, the total error also is normalized defining it as

$$\xi_{\text{tot}} = \frac{1}{3} (\xi_Z + \xi_R + \xi_T). \quad (3)$$

In order to minimize ξ_{tot} , it is considered as a N -dimensional variable. This is the case because the moving windows, used for normalizing the noise functions, are selected independently, one for each station. The point of minimum error is found using the centres of the 5 Hz windows as coordinates of a N -dimensional uniform grid, with points spaced apart 0.3 Hz.

Fig. 7 shows the solutions, using EQ5 as a calibration earthquake, for the three stations of Tungurahua volcano. The values along each axis are window centres. Therefore, the site FRF are constructed normalizing the noise functions with reference levels that are equal to the mean amplitudes of the ranges [4.2, 9.2] Hz (BCUS), [4.8, 9.8] Hz (BMAS1) and [6.0, 11.0] Hz (BRUN), with ± 0.15 range

error, determined by the grid resolution. Fig. 8 shows vertical, radial and transverse components of EQ5 before and after removing the site effect. For comparison, the traces of each subplot were plotted at the same scale. Before site corrections the BRUN components are larger than BMAS1 and BCUS, while horizontal components of BMAS1 are larger than BCUS components (Fig. 8a).

3.4 Method evaluation

After removing the site effects, the signals of a distant earthquake should be the same on each station. In practice, the differences between stations, for each component, should be minimal. This is confirmed in Fig. 8 for EQ5, where is apparent the improvement after the site corrections. This is an expected result because EQ5 was used to normalize the seismic noise spectra, however, the method still needs to be evaluated with earthquakes that have not participated in the FRF construction, EQ1–EQ4.

We can evaluate the errors between stations before and after removing the site effects using the eqs (2) and (3). Table 3 summarizes their values for EQ1–EQ5 earthquakes (EQ5 is the calibration earthquake). Columns labelled with an ‘s’ added to the earthquake name, collect errors after removing the site effects.

With the exception of the vertical components of EQ3 and EQ4, the errors of all components decrease. ξ_{tot} improves in all cases after removing the site effects. This fact suggests that EQ1–EQ4 could also be used as calibration events.

3.5 Method sensitivity

We can compare EQ1–EQ5 calibrations to gauge the method sensitivity. It is clear that the reference level values could depend on the selected calibration earthquake. This is evaluated with the change of ξ_{tot} before-after removing the site effects, defined as the relative improvement $\bar{\xi} = [\xi_{\text{tot}}(\text{before}) - \xi_{\text{tot}}(\text{after})] / \xi_{\text{tot}}(\text{before})$. A positive $\bar{\xi}$ represents an improvement of the similarity of the signals, a negative represents a worsening, and a value around zero reflects non significant changes. Table 4 shows $\bar{\xi}$, where each column is related to the selected calibration earthquake. The final row is the sum of $\bar{\xi}$,

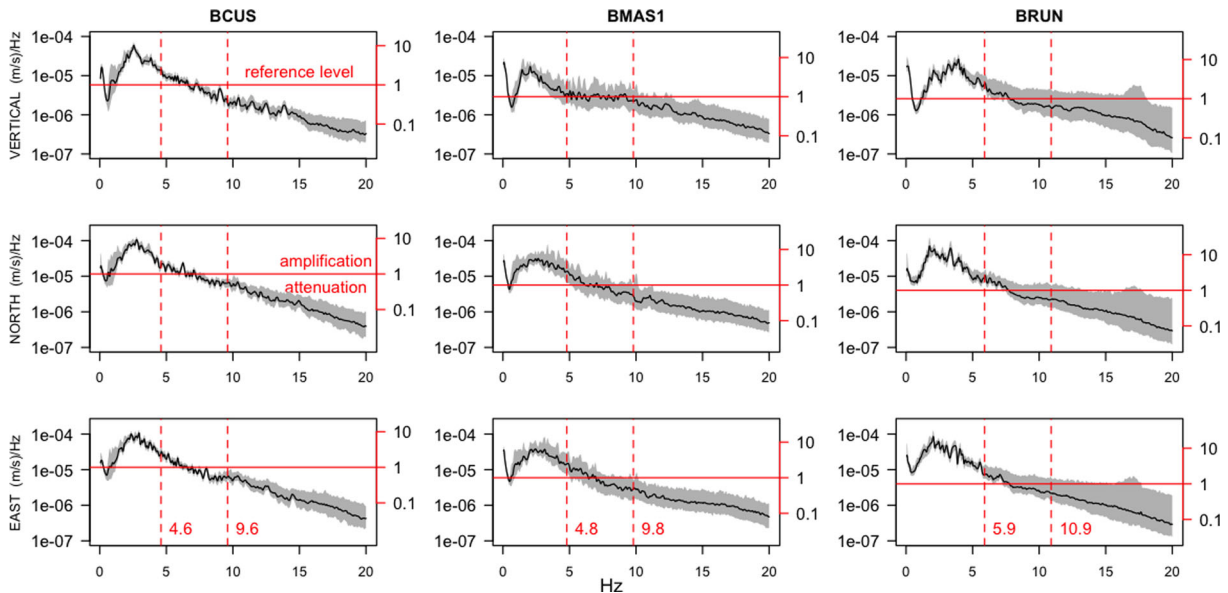


Figure 5. Seismic noise spectra [$\text{m s}^{-1} \text{Hz}^{-1}$] used to construct site frequency response functions (FRF). Grey regions are 95 per cent variation intervals. Solid black lines are medians. Vertical red dashed lines are borders of a evaluation range, a 5 Hz length moving window. Solid red lines are reference levels computed as average amplitude of the moving window. The right vertical axes are the FRF values (dimensionless) after the noise normalization.

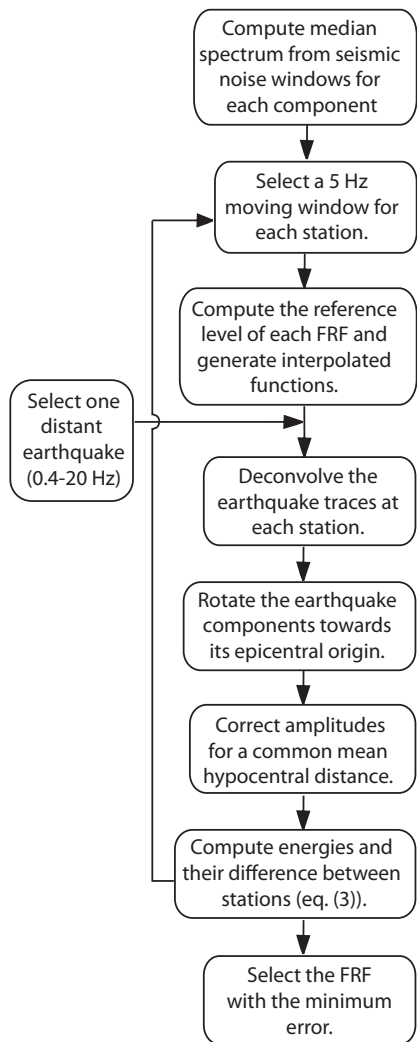


Figure 6. Flow chart of the process to compute the site frequency response functions.

a measure that gives an idea of which calibration earthquake could be better.

When EQ3 and EQ4 are used as calibration earthquakes, the lowest relative improvements are obtained. This fact can be observed for the whole set EQ1–EQ5 (last row in Table 4), as well as for each earthquake. When EQ3 is used, the ξ_{tot} minimization gives a solution at grid borders. It means that the optimal solution in not

well constrained. The solution for EQ4 are the intervals [3.6, 8.6] Hz (BCUS), [4.8, 9.8] Hz (BMA51) and [5.1, 10.1] Hz (BRUN). In both cases, the low relative improvements are due to a worsening of the vertical component, although the horizontal components were improved (Table 3). We consider that only EQ1, EQ2 and EQ5 earthquakes are suitable as calibration earthquakes, since they always shows positive relative improvements. Table 5 shows their intervals used to construct the site FRF, and their averages for each station which are shown as dashed vertical lines in Fig. 5. We next go on to use these average values to make a number of applications.

4 APPLICATIONS

4.1 Decoupling explosion signals

When an volcanic explosion occurs, seismic and acoustic waves are generated. Because the wave velocity in air is less than that in the Earth, the acoustic arrival is recorded by the seismic sensor at a later time than the seismic arrival, when the air wavefront impacts on the soil. Similarly to other impacts that occur on the surface, such as pyroclastic flows or Lahars, a high frequency content in its signal is expected. These high frequencies are attenuated relatively quickly, but are still recorded by the sensor because it is buried at a shallow depth. In addition, the acoustic impact should produce similar effects on all seismic components. However, frequently its signature is observed more clearly on the vertical component than on the horizontals. Fig. 9(a) shows a case where the acoustic impact is hidden by the seismic signals, even though the explosion is of a moderate size. Fig. 9(b) shows the same signals after removing the site effects; the acoustic arrivals are now clearly visible on all components.

The inverse site FRF can be considered as a selective filter that modifies only those amplitudes that deviate from their reference levels (Fig. 5). Small amplitude changes are observed in all stations at low frequencies, roughly around 0.3–1.1 Hz, and at high frequencies, between 5 and 11 Hz. Amplitudes at frequencies between 1 and 5 Hz are attenuated gradually, while those at frequencies larger than 11 Hz are amplified. Explosion source mechanisms may be related to a mass expansion, mainly producing low frequencies, while acoustic impacts generate signals with dominant high frequencies. Accordingly, the seismic record contains signals from both types of sources, which are easily recognized after removing the site effect (Fig. 9b). Finally, a further filter (high pass or low pass) can be applied to separate the coupled signal from the seismic record.

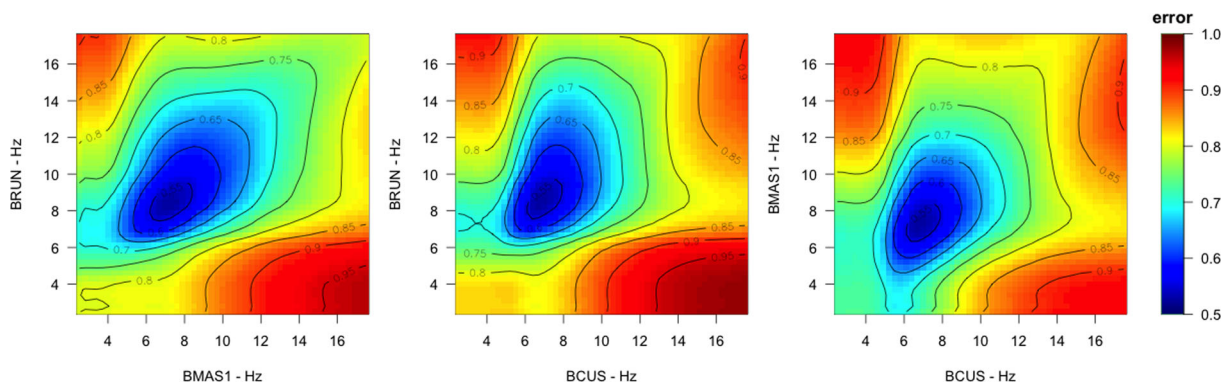


Figure 7. Minimum error that defines optimum windows used to compute the reference level of site response functions: BCUS [4.2,9.2], BMA51 [4.8,9.8], BRUN [6.0,11.0] Hz.

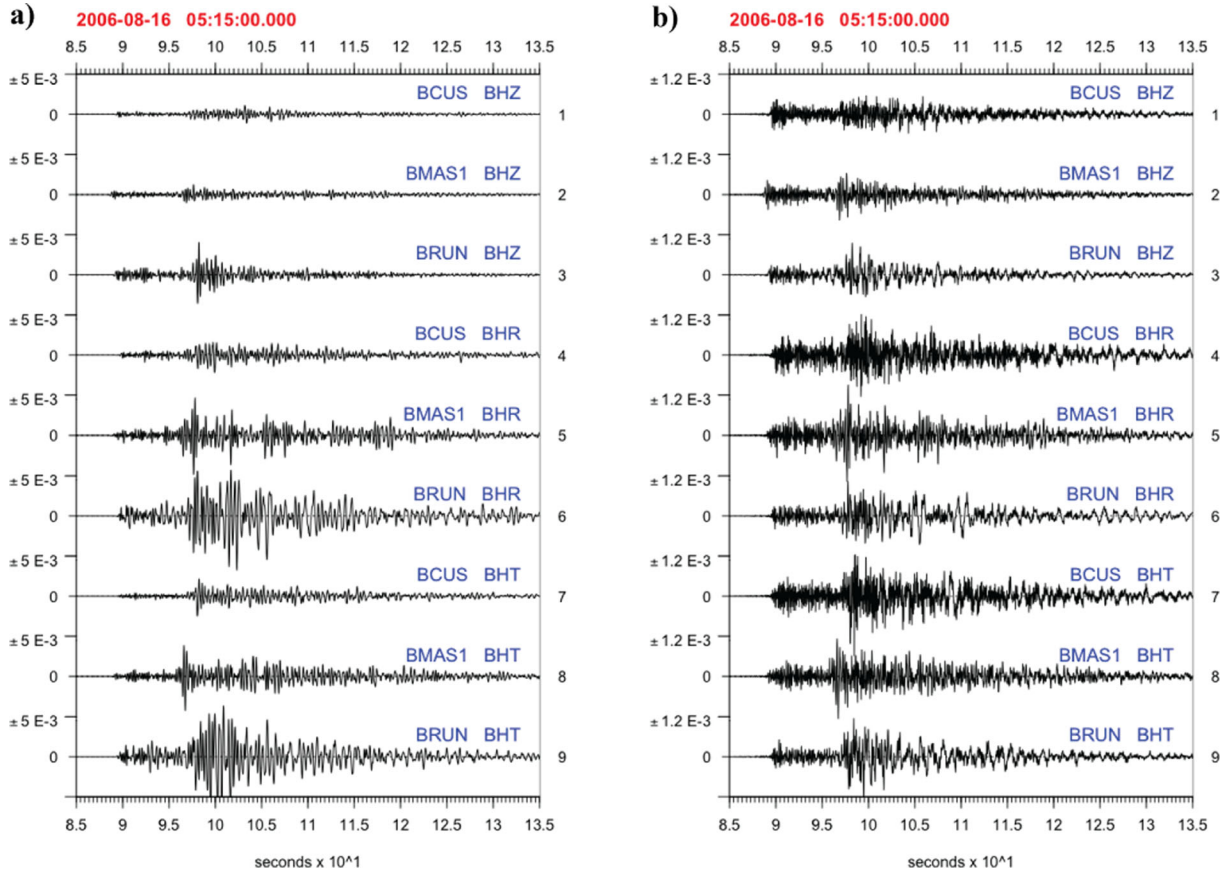


Figure 8. Vertical (BHZ), radial (BHR) and transverse (BHT) velocity components (m s^{-1}) of EQ5 earthquake (a) before and (b) after removing site effects.

Table 3. Energy errors (eq. 2) for each seismic component before (columns EQx) and after (columns EQxs) site corrections. EQ5 has been used as calibration earthquake.

| Error | EQ1 | EQ1s | EQ2 | EQ2s | EQ3 | EQ3s | EQ4 | EQ4s | EQ5 | EQ5s |
|--------------------|------|------|------|------|------|------|------|------|------|------|
| ξ_Z | 0.60 | 0.45 | 0.62 | 0.54 | 0.36 | 0.55 | 0.45 | 0.49 | 0.60 | 0.54 |
| ξ_R | 0.60 | 0.43 | 0.65 | 0.47 | 0.65 | 0.49 | 0.67 | 0.49 | 0.68 | 0.52 |
| ξ_T | 0.66 | 0.45 | 0.65 | 0.46 | 0.68 | 0.57 | 0.68 | 0.51 | 0.67 | 0.54 |
| ξ_{tot} | 0.62 | 0.44 | 0.64 | 0.49 | 0.56 | 0.54 | 0.60 | 0.50 | 0.65 | 0.53 |

Table 4. Relative improvement $\bar{\xi}$ for each earthquake (row) when one of them (column) is used as calibration earthquake.

| | EQ1 | EQ2 | EQ3 | EQ4 | EQ5 |
|-----|------|------|-------|-------|------|
| EQ1 | 0.32 | 0.30 | 0.18 | 0.18 | 0.28 |
| EQ2 | 0.27 | 0.28 | 0.09 | 0.17 | 0.23 |
| EQ3 | 0.08 | 0.05 | 0.23 | -0.11 | 0.05 |
| EQ4 | 0.12 | 0.12 | -0.04 | 0.21 | 0.17 |
| EQ5 | 0.17 | 0.16 | 0.06 | 0.13 | 0.18 |
| Sum | 0.96 | 0.91 | 0.52 | 0.58 | 0.91 |

Fig. 10 presents the spectrograms of the east component at BCUS station before (a) and after (b) removing the site effects. Using the same colour scale for the power spectral density, the acoustic arrival (the coupling) is clearly observed in Fig. 10(b) at frequencies over 7 Hz, while the seismic signal has dominant energy content below 4 Hz. Exploring the other explosions of this study, the threshold 4 Hz appears to be a suitable level to separate the coupled signals.

Table 5. Normalization intervals (Hz).

| | BCUS | BMAS1 | BRUN |
|---------|------------|------------|------------|
| EQ1 | [5.1–10.1] | [5.1–10.1] | [6.3–11.3] |
| EQ2 | [4.5–9.5] | [4.5–9.5] | [5.4–10.4] |
| EQ5 | [4.2–9.2] | [4.8–9.8] | [6.0–11.0] |
| Average | [4.6–9.6] | [4.8–9.8] | [5.9–10.9] |

4.2 Location and VASR of explosions

VASR is the ratio of acoustic to seismic source energies and their estimation depend on the source locations. The importance of this measure is that it may be related to different explosion mechanisms and their physical interpretations may be useful to compare processes at an individual or various volcanoes (Johnson & Aster 2005). In this section, we compare the seismic source locations and VASR results, before and after removing the site effects, for a set of twenty explosions recorded on 2006 July 20–21. Each one of these events has a short duration, lasting a few tens of seconds, while

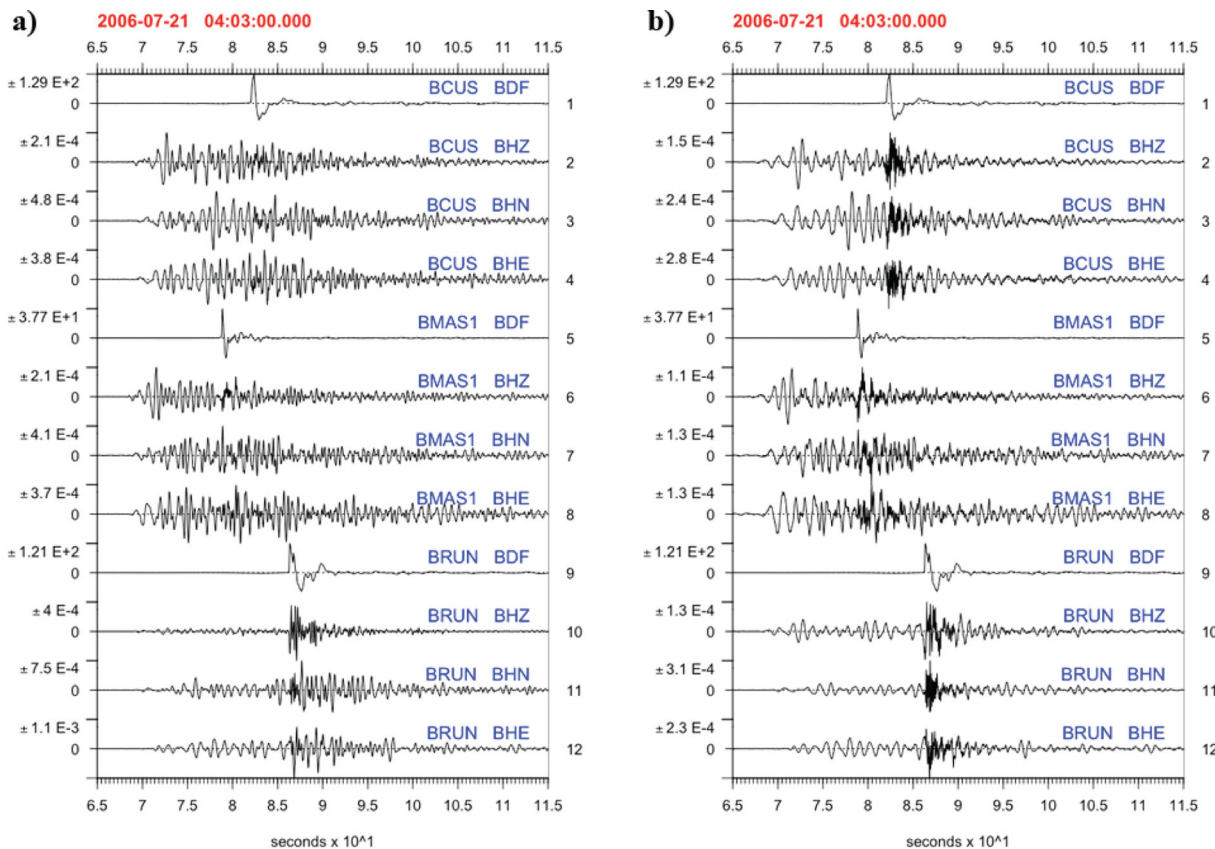


Figure 9. Acoustic pressure changes (BDF – Pa) and seismic velocities (BHZ, BHN and BHE – m s^{-1}) of an explosion on 2006 July 21 at 04:04 UTC, (a) without removing the site effects and (b) removing them. The acoustic signals associated with an explosion are easily seen on the seismic traces after the site effect is removed.

a sustained eruption, what we call a jet, is considered in the next section.

Explosions are shallow fragmentation processes that could be triggered by gas migration, as analogue experiments suggest (Mader *et al.* 1996), and stress–strain models and field observations confirm (Lyons *et al.* 2012; Nishimura *et al.* 2012). However, a second mechanism where a deep source generates waves that propagate along the conduit, reach the summit and trigger an explosion (Nishimura & Chouet 2003) has been observed and modelled at Tungurahua volcano (Kumagai *et al.* 2011; Kim *et al.* 2014). After removing the site effects, Fig. 11(b) shows seismic sources located 1–3 km below the summit. The difference with Fig. 11(a) is caused only by the site effect corrections.

Our location method employs an initial $20 \times 20 \times 20$ km grid, with 1 km node spacing and bounded by the topographical surface. Assuming a seismic source at each node, the energy $\mathcal{E}_i = \int E_i(f) df$, is computed after correcting the intensity recorded at each station i , with the elastic and inelastic factors (eq. 5). Because the source energy should be the same after comparing different stations, the best location is the node that produces a minimum difference between the computed energies, measured by the following normalized error function:

$$Err = \frac{2}{N(N-1)} \sum_{i>j} \frac{\sum_f |E_i(f) - E_j(f)|}{\sum_f E_i(f) + \sum_f E_j(f)}, \quad (4)$$

where the integrals in the spectral domain have been approximated with sums, N is the number of stations, $E_i(f)$ are accumulated source energies, every 0.1 Hz, summing all seismic components. Progressively finer grids are constructed and evaluated sequentially around the best location identified in the previous coarser grids.

The new grid is constructed around the previous solution with dimensions $8 \times 8 \times 8$ times the previous node distance, but with a new node distance equal to the half of the previous one (e.g. second grid: $8 \times 8 \times 8$ km with node distance 0.5 km; third grid: $4 \times 4 \times 4$ km with node distance 0.25 km; etc.). The sequence stops when the change of the normalized error is less than 0.1 per cent of the previous error value. Locating our set of explosions required between 2 and 4 grids.

The seismic records were filtered below 4 Hz to minimize or decouple the impact of the air waves on the stations. The traces were cut in a window that started between 3 and 5 seconds before the seismic arrivals, ending between 60 and 100 s later, depending on the event. The total seismic source energy \mathcal{E}_i was obtained assuming a spherical source, isotropic radiation pattern, and correcting the recorded intensities with the elastic and inelastic attenuation factors (Aki & Richards 2002):

$$\mathcal{E}_i = \int_0^4 E_i(f) df = \Omega r_i^2 \rho c \int_0^4 v_i^2(f) \exp\left(\frac{2\pi f}{Qc} r_i\right) df, \quad (5)$$

where $\Omega = 4\pi$ sr the solid angle available for the seismic wave radiation, ρ is the Earth density, c the wave velocity, r_i the source–station distance, $v_i^2(f)$ the power spectral density of recorded velocities of all components [$v_i^2(f) = v_{Zi}^2(f) + v_{Ni}^2(f) + v_{Ei}^2(f)$], and Q the quality factor. For Tungurahua volcano we have selected $\rho = 2500 \text{ kg m}^{-3}$, $c = 2000 \text{ m s}^{-1}$ (Kumagai *et al.* 2011) and $Q = 40.6$. The S -wave velocity is used as c assuming that P – S scattering conversions occurs more easily in a highly heterogeneous

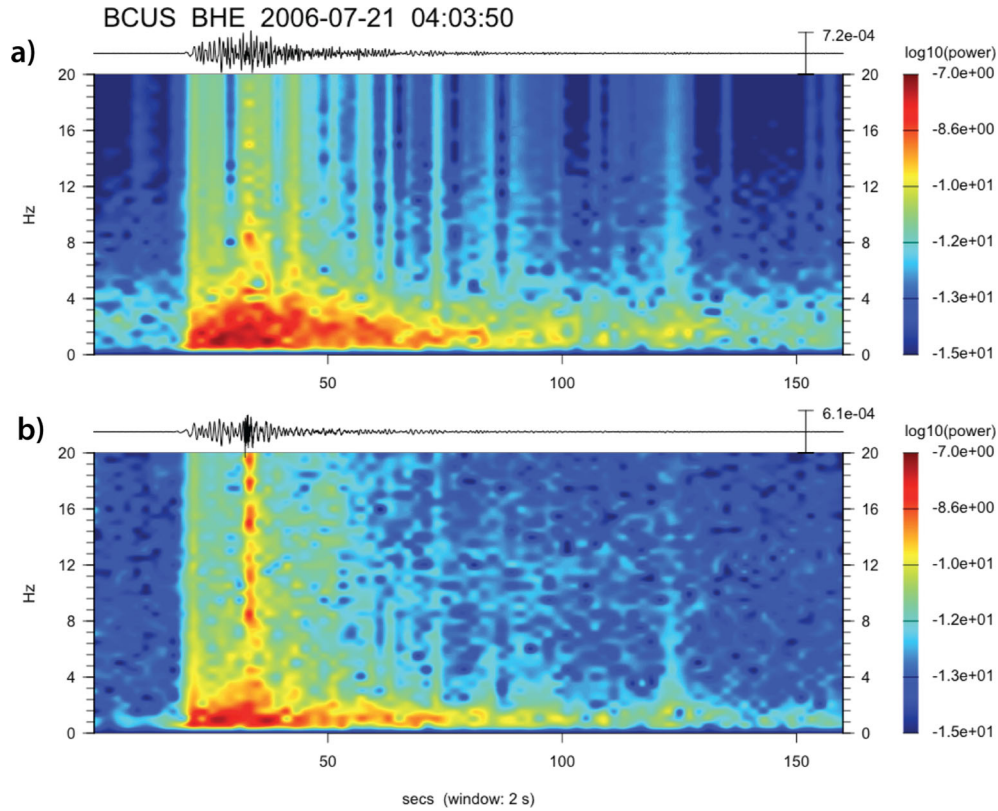


Figure 10. Power spectrograms [(m s⁻¹)² Hz⁻¹] of BHE component at BCUS station of an explosion: (a) before and (b) after removing the site effects.

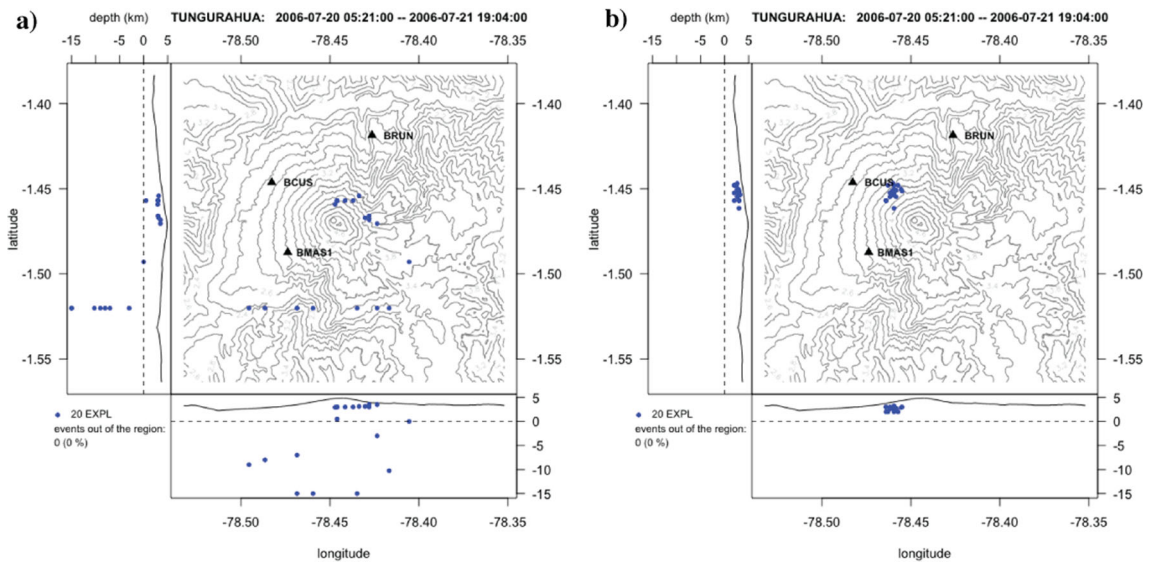


Figure 11. Location of 20 explosions (a) before and (b) after removing the site effects.

medium than *S*–*P* conversions (Aki 1992; Kumagai *et al.* 2011). The factor $\Omega\rho c$ cancels out in eq. (4), without effects on the location solution. However, the quantity Q_c within the inelasticity factor can modify the solutions. Q may be frequency dependent, but we are assuming that it is a constant that characterizes the average energy absorption of the medium. To constrain the Q value we use the clustering properties of the solutions. Due to the short time between explosions (minutes to hours) they were likely generated in a limited spatial region (e.g. Kim *et al.* 2014). Computing the mean distance from the explosion locations to the cluster centre, and defining it as

the median of the locations, we choose Q that produces a minimum cluster mean distance. Fig. 12 shows the cluster mean distance as function of Q with $c = 2000 \text{ m s}^{-1}$ for both cases, before (black line) and after (red line) removing the site effects. The optimum quality factor is $Q = 40.6$ ($Q_c = 81.2 \text{ km s}^{-1}$) for the frequencies less than 4 Hz.

The VASR for the explosions is also very sensitive to the site effects. The black circles in the Fig. 13 are computed assuming that the seismic and acoustic sources are located at the summit, without removing the site effects; whereas the black triangles are obtained

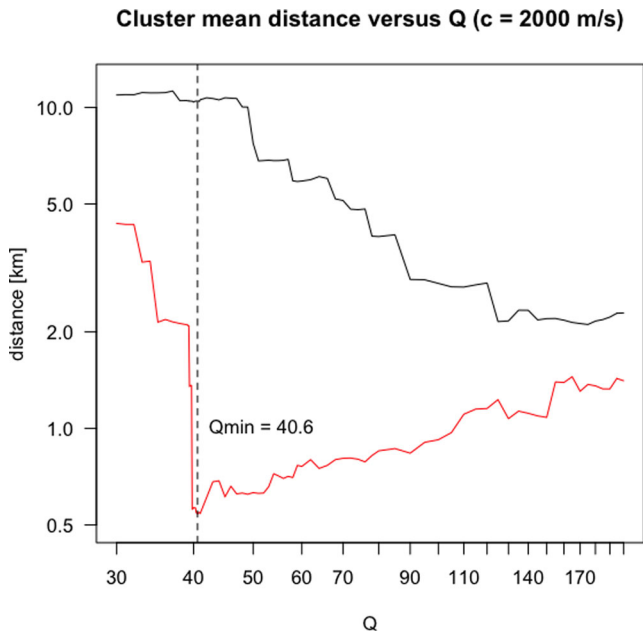


Figure 12. Cluster mean distance of explosion locations versus Q , before (black solid line) and after (red solid line) removing the site effects.

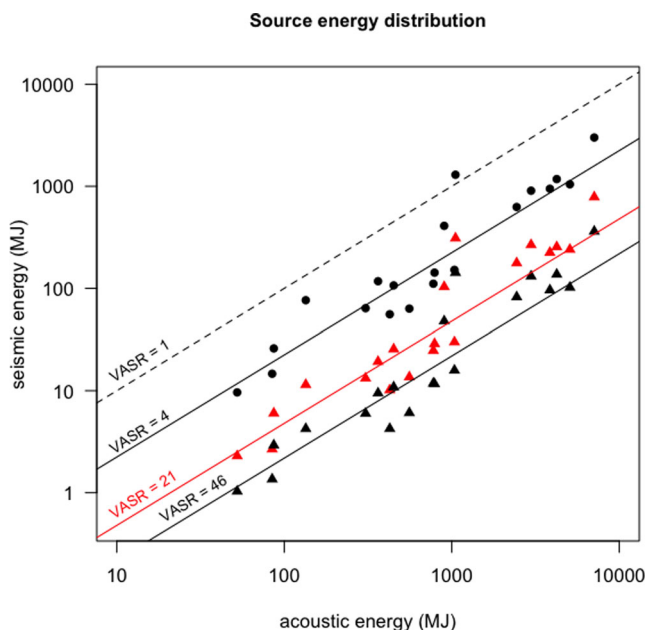


Figure 13. Distribution of seismic and acoustic energies (MJ) for sources located at the volcanic crater, before (black circles) and after (black triangles) removing site effects. Red triangle distribution is obtained after removing site effects and using the locations plotted in the Fig. 11(b). The solid straight lines are the mean VASR of the distributions. The black dashed line is the level where the acoustic and seismic energies are equal.

removing the site effects using the same location. For this case, the differences obtained in the VASR values is one order. The red triangles are obtained by computing the seismic energies with the eq. (5), after removing the site effects and using their calculated locations (Fig. 11b). The differences between the mean VASR of these three distribution sets (solid straight lines), are statistically significant. The source seismic energy computed for the fix location at the crater (black symbols) considered only elastic attenuation ($Q^{-1} \rightarrow 0$), $\Omega = 4.1$ sr (due to the Tungurahua's cone shape: 3 km re-

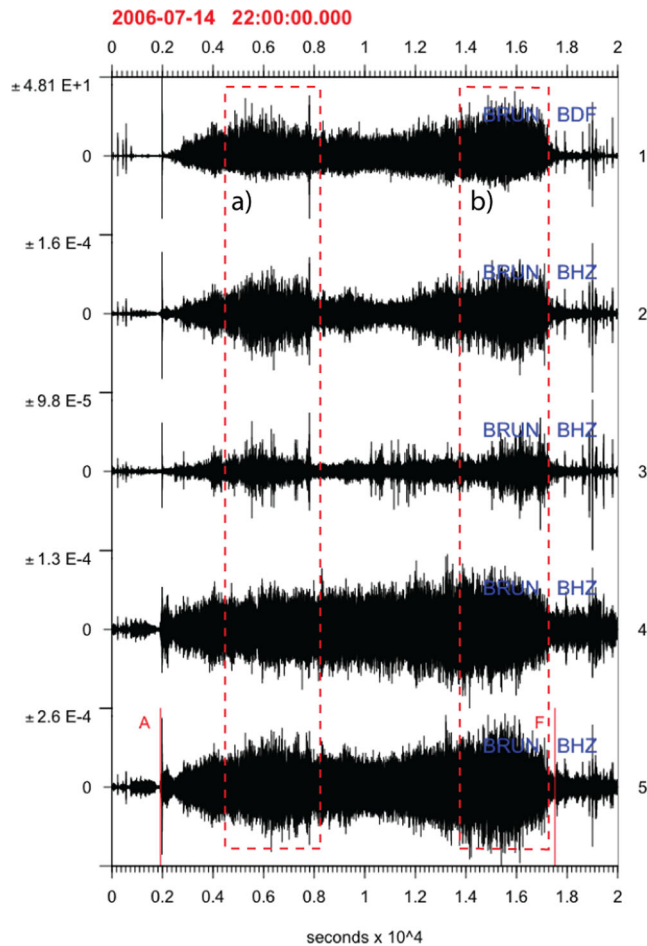


Figure 14. Acoustic pressure change (trace 1, BDF – Pa) and several filters of the vertical (BHZ – m s^{-1}) seismic velocity records, at BRUN station, of 2006 July 14–15 eruption. Trace 2: 4–20 Hz filter of BHZ, without removing site effects. Trace 3: 4–20 Hz filter of BHZ, after removing site effects. Trace 4: BHZ after removing site effects. Trace 5: BHZ without removing site effects (original trace). Dashed boxes (a) and (b) spot time periods discussed in the text.

ief height and a 8 km radius) $\rho = 2500 \text{ kg m}^{-3}$ and $c = 2000 \text{ m s}^{-1}$. The source acoustic energy \mathcal{E}_{ai} , at the station i , is computed with only an elastic correction:

$$\mathcal{E}_{ai} = \frac{\Omega_a r_i^2}{\rho_a c_a} \int p_i^2(t) dt, \quad (6)$$

where $\Omega_a = 8.5$ sr, while the air density and wave velocity $\rho_a = 1.25 \text{ kg m}^{-3}$, $c_a = 337 \text{ m s}^{-1}$, are obtained for an average temperature of 10°C around Tungurahua volcano. The term p_i represents the acoustic pressure change recorded at the station i .

4.3 2006 July 14–15 eruption jet

The first eruption that produced pyroclastic flows since 1999 in Tungurahua volcano began At 22:32 UTC on 2006 July 14. It lasted roughly 4.3 hr and produced a 15 km height column over the summit (Molina *et al.* 2006; Kumagai *et al.* 2007). Fig. 14 shows the acoustic component (BDF, trace 1) and several filters of the vertical seismic component (BHZ, traces 2–5) at station BRUN. Traces 5 and 4 are records before and after removing the site effects, respectively; Fig. 15 shows their spectrograms. Trace 2 is a 4 Hz high pass filter of trace 5, while trace 3 is a 4 Hz high pass filter of trace 4.

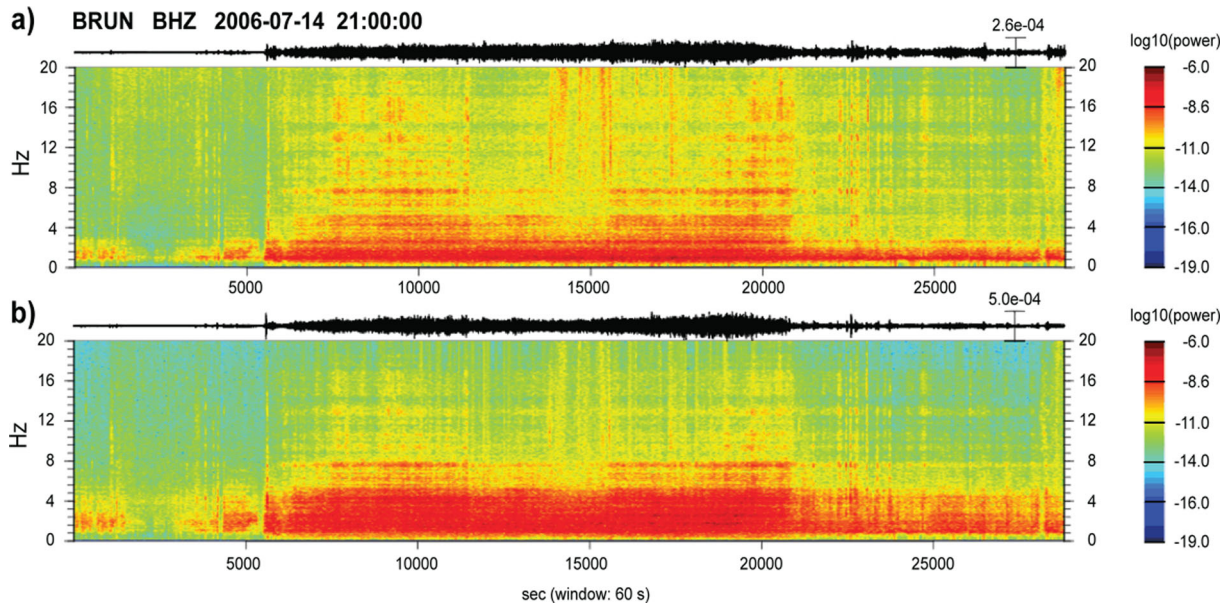


Figure 15. Power spectrograms of the vertical component (BHZ) at BRUN station of 2006 July 14–15 eruption: (a) after site corrections and (b) without site corrections.

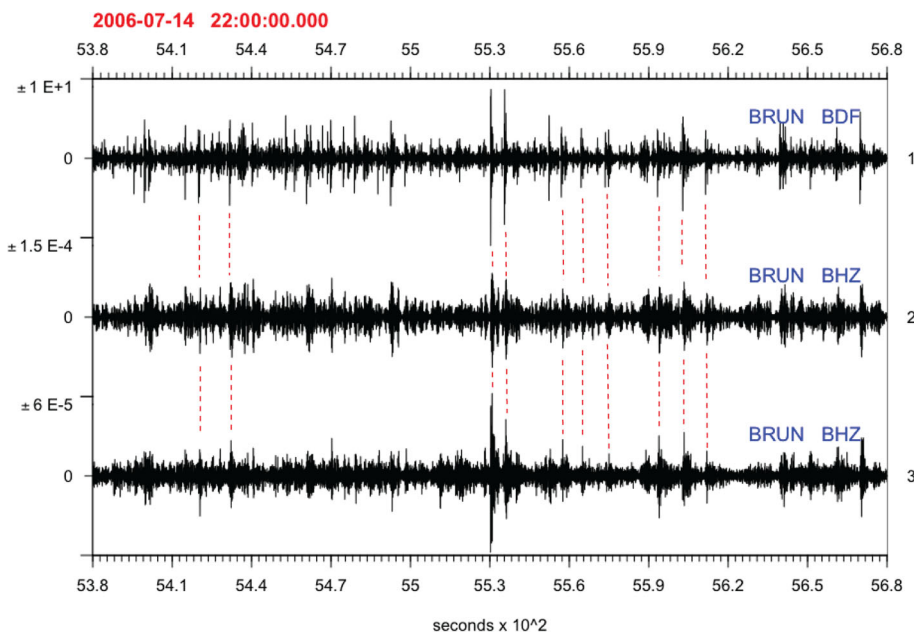


Figure 16. A 5-min window of acoustic pressure change (BDF – Pa) and vertical (BHZ – $m s^{-1}$) seismic velocity records from the eruption jet, before (trace 2) and after (trace 3) removing site effects. All signals are filtered over 4 Hz. Vertical dashed lines spot several explosions.

Within the time period surrounded by red dashed boxes, (a) and (b) in Fig. 14, the acoustic signals reach their highest amplitudes. Their coupling effect appears as a progressive increase of seismic amplitudes in the traces without site corrections (2 and 5). Such coupling is not evident after the site correction (trace 4), which suggests that the arriving seismic waves, caused by the internal tremor, are larger than coupled waves.

Fig. 16 shows a 5 minute window of traces 1, 2 and 3 within the box marked (a) on Fig. 14. Here, the acoustic trace has been high pass filtered over 4 Hz. Red dashed lines spot several explosions

where the signal to noise ratio seems to be higher after removing the site effects (trace 3), than just filtering the signal with high frequencies (trace 2).

To investigate the air wave coupling (Ichihara *et al.* 2012) the cross-correlograms of vertical seismic and acoustic components at BRUN station, were computed (Fig. 17). If the data are only filtered at high frequencies, the coupling appears clearly (Fig. 17a). Fig. 17(b) shows a first approximation for separating the internal seismic tremor only filtering the traces at low frequencies. However correlations around 0.40 are still visible in the signals.

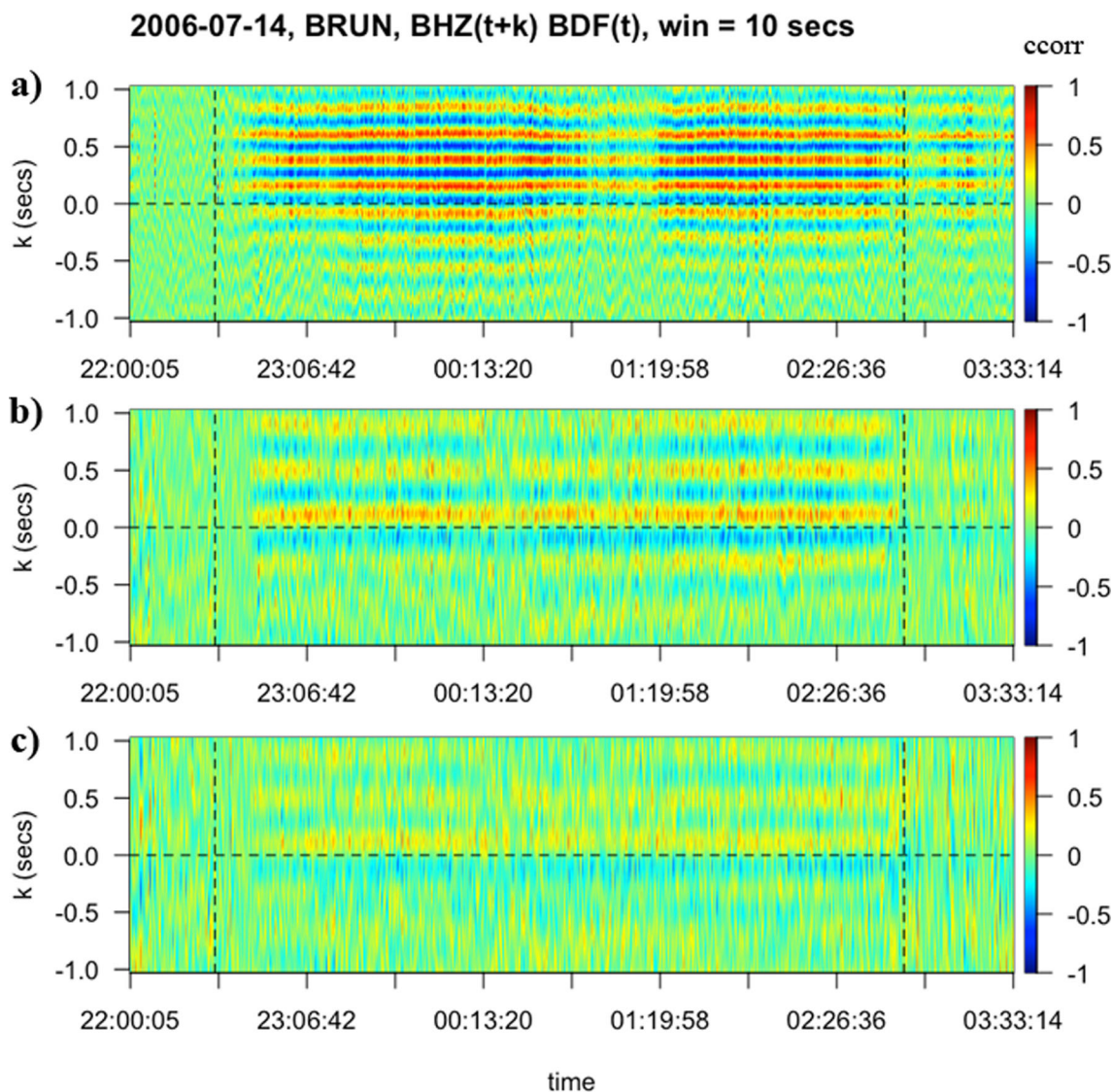


Figure 17. Cross-correlograms of seismic (BHZ) and acoustic (BDF) components at BRUN station of 2006 July 14–15 eruption: (a) without removing site effects and applying a 4 Hz high-pass filter on both records, (b) without removing site effects and applying a 4 Hz low-pass filter on both records, and (c) removing site effects and using a 4 Hz low-pass filter on both records. In all cases zero-shift filters were used. k is the delay, in seconds, of the seismic component. A non overlapped 10 second moving window was used. Vertical dashed lines point to the initial and final jet time (22:32 on 14 July and 02:52 on 15 July), which are the same limits that appear as solid red lines of trace 5 in Fig. 14.

After removing the site effects (Fig. 17c) the cross-correlations are weak, with values around 0.25 or less, suggesting that removing site effects significantly helps reduce coupling effects during the jet activity.

5 DISCUSSION

5.1 Physical assumptions

Previously proposed methods for site correction are based on assumptions either that the structure beneath a reference station has a low wave distortion (e.g. Kato *et al.* 1995), or that the vertical components do not change as function of depth (e.g. Nakamura 1989). Deconvolving the records with the first assumption is equiv-

alent to transforming each site, forcing it to be as similar as possible to the reference one. With the second assumption, the horizontal components are forced to be similar to the vertical one, which produce an artificial incident angle of 45° . Both cases have physical limitations. Although in the first case, the reference station could be installed on a lava flow (a high velocity material), in a volcanic environment is likely that there will be various layers beneath the site, that can strongly distort the signals. While in the second case, we might expect different responses for the vertical and horizontal components because the underlying layer dimensions are larger horizontally than they are vertically. Our method does not make these assumptions. Instead, we use the principle that the signal of a far earthquake should be similar for all stations after site corrections. For example, Figs 8 and 9 show that after the site corrections the vertical components remain smaller than the horizontals. The

horizontal to vertical ratios depend only on the incident angle of the incoming wave.

5.2 Physical interpretations

What is the physical interpretation of the frequency bands given in Table 5 used in the site FRF construction? Studying the Tottori-Ken Seibu earthquake ($6.6 M_w$), that occurred in 2000 in Japan, Take-mura *et al.* (2009) demonstrated that the *S*-wave radiation pattern could be affected by medium heterogeneities that scatter seismic waves, generating an isotropic pattern. This physical process is frequency dependent. The authors found that the radial and transversal components have similar amplitudes for 4–8 Hz waves, whereas their differences increase for lower frequency waves. Based on this interpretation Kumagai *et al.* (2010), studying Cotopaxi and Tungurahua volcanoes, justifies the use of frequencies 5–12 Hz to get better seismic source locations. Similarly, Battaglia & Aki (2003) studying Piton de la Fournaise volcano, found that the best source locations were obtained by filtering the signals in 5–10 Hz. Although scattering is one of the physical processes expected in a heterogeneous medium, we propose a complementary physical interpretation.

The site correction factors computed by Kumagai *et al.* (2010) used the coda method, with a reference station, and overlapping 5 Hz width frequency bands. A site correction with these average factors can be considered as a first approximation. However, two sites can have similar average factors but different site responses. In this case, remanent site effects would be left in the corrected signals. Thus the details of the site responses showed in Fig. 4, especially at low frequencies, would not be taken into account using the averaging procedure of the coda method. Therefore, the subsequent use of a 5–12 Hz pass band to improve the source locations only considers the scattered energy, and all remanent site effects at low frequencies are filtered out. This procedure also removes any low frequency source energy.

We interpret our noise-based FRF (Fig. 5) in the following way. The frequency bands 4.6–9.6 Hz (BCUS), 4.8–9.8 Hz (BMAS1) and 5.9–10.9 Hz (BRUN) of the inverse FRF define where amplitudes are roughly constant around the window centres; this is consistent with the hypothesis that energy in these frequency ranges is related to scattered energy. Below 5 Hz the recorded signals are corrected, attenuating them gradually, assuming that the site amplifies the waves by refractions or constructive interference. However, it is worth noting that the three sites here studied show that around 0.3–1.1 Hz the signals are not significantly distorted. Finally, amplitudes larger than 11 Hz are amplified, assuming that the sites dissipate this energy mainly due to energy absorption by the medium. Therefore, our site correction applies across a broad frequency range, minimizing site effects and taking into account several physical processes. It is worth noting that Battaglia & Aki (2003) and Kumagai *et al.* (2010) used a common frequency band for all stations to obtain the source locations. However, we use non common bands, because we interpret each one as a site property that defines each site FRF.

5.3 Comparison of methods and restrictions

Any proposed method should be assessed by both comparing its results with other methods and evaluating its sensitivity when one or more parameters change. Ideally, two data sets should be used;

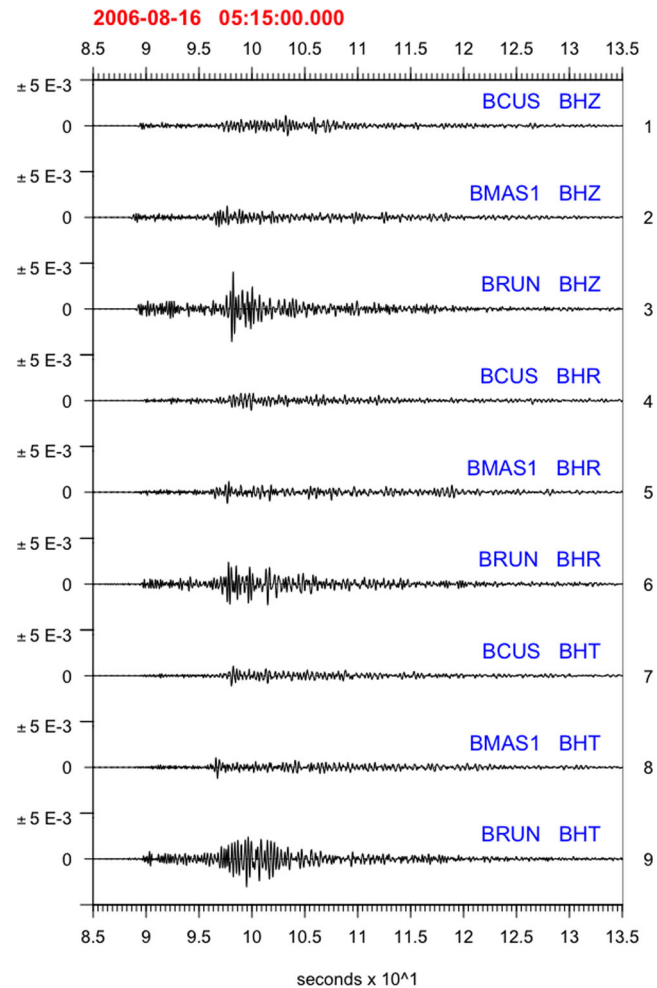


Figure 18. EQ5 earthquake (Fig. 8a) after site effect corrections using H/V ratio method.

one for calibrating or computing the required parameters and another for applying and testing the results. Although the assessment and comparison of methods is not a goal of this study, we have described the procedure for it. Eqs (2) and (3) might also be used to evaluate other methods, while their sensitivity is dependent on the amount of data available. In our case, we have found that, at least using EQ1, EQ2 and EQ5 as calibration earthquakes, the reference levels of FRF do not change strongly, as is inferred from the similarity of the obtained normalization intervals (Table 5).

As an example of method comparison and to highlight the consequences of the H/V method, we apply it to the EQ5 earthquake (Fig. 8a). Therefore, we use the median of the seismic noise ratios North/Vertical and East/Vertical in the Fig. 4 as site FRF. Fig. 18 shows the results; only the horizontal components appear modified, and the differences at each component between stations are larger than those obtained by the method here proposed (Fig. 8b). Because of the H/V method is applied to each station without the information of the other ones, and it tends to produce horizontal components with similar amplitude than the vertical, the proportion between vertical components are *transferred* to horizontal components. Roughly, from Fig. 18, the vertical component at BRUN station is between two and three times larger than

the vertical components of BCUS or BMAS1, proportions that are transferred to radial and transversal components. In general, if significant differences are observed in vertical components of distant earthquakes, the H/V ratio method is not suitable for site corrections.

The main restrictions to apply the method here proposed are: (1) the existence of distant earthquakes to normalize the FRF; (2) the confirmation of the frequency range where the seismic noise at different stations can be considered independent; for instance, if several stations are installed close enough each other to be considered on the same geological setting, the information could be the same and the noise coherence high and (3) due to in the normalizing process the search grid dimension increases exponentially with the number of stations, obtaining the optimal solutions depends on the computation capabilities.

5.4 Seismic source location

Assuming a spherical seismic source, we have located a set of explosions with and without removing the site effects, and after decoupling the acoustic signals. As a consequence, we have been able to use the whole seismic traces filtered in the range below 4 Hz, which is, roughly, the expected frequency range for fluid movements (e.g. Nakano & Kumagai 2005). The location procedure is based on the minimization of the differences between the spectral densities of the energies, which includes the information of all components. The advantage of this is observed when the estimation of the absolute seismic source energy is required, such as in the computation of VASR. Large differences are observed in the location results, before and after removing the site effects (Fig. 11), which suggest a strong site influence in the recorded signals. Those locations depend on the elastic and inelastic energy corrections. Furthermore, the product of the quality factor, Q , and the wave velocity, c , controls the amount of energy dissipated as heat and, therefore, the estimation of the energies could change, modifying the locations. We acknowledge that using average values for these factors produce results that might be considered as a first approximation. However, assuming that the explosion set has a common source region, we have explored the impact in the location quality when Q changes (Fig. 12). The best locations were obtained with $Q = 40.6$ (0.4–4.0 Hz), which is comparable to Q values used in other volcanic regions, for instance $Q = 50$ (3 and 7.5 Hz) for Piton de la Fournaise volcano (Battaglia & Aki 2003), $Q = 60$ (5–12 Hz) for Cotopaxi and Tungurahua volcanoes (Kumagai *et al.* 2010), and $Q = 60$ (7–12 Hz) for Taal volcano (Kumagai *et al.* 2013). The cluster appears beneath the north-western flank, but the locations might be influenced by the lack of azimuthal coverage of the July–August 2006 seismic network. Nevertheless, there are cases in Tungurahua showing explosions at the surface triggered by deep perturbations, located roughly beneath the summit, but then followed by tremors with locations that are relatively close to our locations (compare fig. 1b in Kumagai *et al.* 2011, with our Fig. 11b). This suggests the existence of a region that is not beneath the summit and may also be a perturbation source of our explosions.

5.5 VASR and coupling of signals

Although changes in VASR could be related to physical processes, we have found that the influence of site effects is significant. For

our set of explosions, removal of the site effects causes a change of one order of difference in the VASR values (Fig. 13). The origin of this lies in the amplification of low frequency components of the signals, roughly below 5 Hz. The seismic source energy (eq. 5) may be used to clarify this aspect. Because of conservation of energy, the result of eq. (5) should be the same for any selected station. If the waves travel through media of decreasing velocity, an amplitude compensation factor is applied. Therefore, using uncorrected amplitudes in eq. (5) with high velocity values, produces an over estimation of the energy. Although we do not know the velocity model of the stratified medium beneath each station, assuming that the recorded seismic noise stores site information, the site correction of the signals should produce amplitudes only related to high wave velocities (2000 m s^{-1} , as average, for Tungurahua). Additionally, the VASR computation must take into account the source location (Johnson & Aster 2005); in case of Tungurahua is common to find them several kilometres beneath the crater (Kumagai *et al.* 2011; Kim *et al.* 2014). The red triangles in Fig. 13 include this last correction, which show significant differences compared with the corrected or uncorrected signals located at the volcano summit.

Finally, decoupling the acoustic wave impacts (Figs 9, 10 and 17) has been possible after removing the site effects, for two reasons. First, the site modifies both the waves arriving from internal volcanic regions, mainly by refractions and scatterings, and the coupled air waves by backscattering. Therefore, the site correction reconstructs the signals accounting for the effects of both cases, allowing a decoupling of the internal seismic waves, rich in low frequencies, and the soil response dominated by high frequencies. And secondly, if the seismic records actually include physical components of high frequency, as expected for any impact on the ground independent of its origin, the site correction will amplify them, while low frequencies are attenuated gradually, which improve the contrast in the time and spectral domain. However, the decoupling proposed here is not perfect, although its residuals are weak as is observed in Fig. 17(c). It suggests that other factors need to be taken into account to improve the soil response models of volcanic environments (Matoza & Fee 2014). Nevertheless the site correction improves our ability to decouple seismo-acoustic signals.

6 CONCLUSIONS

We have developed a method for removing site effects at three-component seismometers using records of seismic noise. The procedure is calibrated using regional earthquakes and makes no *a priori* assumptions about a preferred site to be used as reference, or on the relative amplitude variations between components. We show that this correction is important in analysis of seismic and acoustic signals, and their coupling, during periods of volcanic explosions and jets. Furthermore, site corrections can lead to significantly improved source locations of volcanic explosions. We have assumed an isotropic source mechanism, but other source type could be generalized, as has been done in previous studies on Tungurahua volcano (Kumagai *et al.* 2010; Kim *et al.* 2014). In general, corrections for site effects will be important for any seismic analysis method that relies on true amplitudes and accurate amplitude ratios between components.

ACKNOWLEDGEMENTS

We are grateful to Hiroyuki Kumagai for an early reading of this study, useful comments, and for establishing seismo-acoustic networks on Ecuadorian volcanoes (Cotopaxi and Tungurahua) through a project supported by JICA (Japan International Cooperation Agency). Comments and criticisms by two anonymous reviewers provoked a substantial improvement. We thanks SENESCYT (Secretaría Nacional de Educación Superior, Ciencia, Tecnología e Innovación) for supporting through the project PIN-08 (Fortalecimiento del Sistema Nacional de Sismología y Vulcanología) and the scholarship 20120069. We thanks staff of IGEPN (Instituto Geofísico de la Escuela Politécnica Nacional) for maintaining the monitoring system, sharing data and providing support. The entire project was developed upon R (R Core Team 2014), version 3.1.1.

REFERENCES

- Aki, K., 1969. Analysis of the seismic coda of local earthquakes as scattered waves, *J. geophys. Res.*, **74**(2), 615–631.
- Aki, K., 1992. Scattering conversions P to S versus S to P, *Bull. seism. Soc. Am.*, **82**(4), 1969–1972.
- Aki, K. & Chouet, B., 1975. Origin of coda waves: source, attenuation, and scattering effects, *J. geophys. Res.*, **80**(23), 3322–3342.
- Aki, K. & Richards, P., 2002. *Quantitative Seismology*, 2nd edn, University Science Books.
- Andrews, D.J., 1986. Objective determination of source parameters and similarity of earthquakes of different size, *Earthq. Source Mech., AGU*, **37**, 259–267.
- Andronico, D., Lo Castro, M.D., Sciotto, M. & Spina, L., 2013. The 2010 ash emissions at the summit craters of Mt. Etna: relationship with seismo-acoustic signals, *J. geophys. Res.*, **118**, 51–70.
- Battaglia, J. & Aki, K., 2003. Location of seismic events and eruptive fissures on Piton de la Fournaise volcano using seismic amplitudes, *J. geophys. Res.*, **108**(B8), 2364, doi:10.1029/2002JB002193.
- Beauval, C. *et al.*, 2013. An earthquake catalog for seismic hazard assessment in Ecuador, *Bull. seism. Soc. Am.*, **103**(2A), 773–786.
- Buttkus, B., 2000. *Spectral Analysis and Filter Theory in Applied Geophysics*, Springer.
- Campillo, M., Gariel, J.C., Aki, K. & Sanchez-Sesma, F.J., 1989. Destructive strong ground motion in Mexico city: source, path, and site effects during great 1985 Michoacán earthquake, *Bull. seism. Soc. Am.*, **79**(6), 1718–1735.
- Clarke, D., Brenguier, F., Froger, J., Shapiro, N., Peltier, A. & Staudacher, T., 2013. Timing of a large volcanic flank movement at Piton de la Fournaise volcano using noise-based seismic monitoring and ground deformation measurements, *Geophys. J. Int.*, **195**, 1132–1140.
- De Angelis, S., Fee, D., Haney, M. & Schneider, D., 2012. Detecting hidden volcanic explosions from Mt. Cleveland Volcano, Alaska with infrasound and ground-coupled airwaves, *Geophys. Res. Lett.*, **39**, L21312, doi:10.1029/2012GL053635
- Drosos, V.A., Gerolymos, N. & Gazetas, G., 2012. Constitutive model for soil amplification of ground shaking: parameter calibration, comparisons, validation, *Soil Dyn. Earthq. Eng.*, **42**, 255–274.
- Field, E. & Jacob, K., 1993. The theoretical response of sedimentary layers to ambient seismic noise, *Geophys. Res. Lett.*, **20**(24), 2925–2928.
- Hagerty, M.T., Schwartz, S.Y., Garces, M.A. & Protti, M., 2000. Analysis of seismic and acoustic observations at Arenal Volcano, Costa Rica, 1995–1997, *J. Volc. Geotherm. Res.*, **101**, 27–65.
- Hall, M.L., Steele, A.L., Mothes, P.A. & Ruiz, M.C., 2013. Pyroclastic density currents (PDC) of the 16–17 August 2006 eruptions of Tungurahua volcano, Ecuador: geophysical registry and characteristics, *J. Volc. Geotherm. Res.*, **265**, 78–93.
- Hartzell, S.H., 1992. Site response estimation from earthquake data, *Bull. seism. Soc. Am.*, **82**(6), 2308–2327.
- Ichihara, M., Takeo, M., Oikawa, J. & Oshimoto, T., 2012. Monitoring volcanic activity using correlation patterns between infrasound and ground motion, *Geophys. Res. Lett.*, **39**, doi:10.1029/2011GL050542.
- Johnson, J.B. & Aster, R.C., 2005. Relative partitioning of acoustic and seismic energy during Strombolian eruptions, *J. Volc. Geotherm. Res.*, **148**, 334–354.
- Johnson, J.B., Aster, R.C., Ruiz, M.C., Malone, S.D., McChesney, P.J., Lees, J.M. & Kyle, P.R., 2003. Interpretation and utility of infrasonic records from erupting volcanoes, *J. Volc. Geotherm. Res.*, **121**, 15–53.
- Kato, K., Aki, K. & Takemura, M., 1995. Site amplification from coda waves: validation and application to S-wave site response, *Bull. seism. Soc. Am.*, **85**(2), 467–477.
- Kim, K., Lees, J.M. & Ruiz, M.C., 2014. Source mechanism of Vulcanian eruption at Tungurahua volcano, Ecuador, derived from seismic moment tensor inversions, *J. geophys. Res.*, **119**, doi:10.1002/2013JB010590.
- Kumagai, H. *et al.*, 2007. Enhancing volcano-monitoring capabilities in Ecuador, *EOS, Trans. Am. geophys. Un.*, **88**(23), 245–252.
- Kumagai, H. *et al.*, 2010. Broadband seismic monitoring of active volcanoes using deterministic and stochastic approaches, *J. geophys. Res.*, **115**, doi:10.1029/2009JB006889.
- Kumagai, H., Palacios, P., Ruiz, M., Yepes, H. & Kozono, T., 2011. Ascending seismic source during an explosive eruption at Tungurahua volcano, Ecuador, *Geophys. Res. Lett.*, **38**, doi:10.1029/2010GL045944.
- Kumagai, H. *et al.*, 2013. Source amplitudes of volcano-seismic signals determined by the amplitude source location method as a quantitative measure of event size, *J. Volc. Geotherm. Res.*, **257**, 57–71.
- Leyes, C., Ley, C., Klein, O., Bernard, P. & Licata, L., 2013. Detecting outliers: do not use standard deviation around the mean, use absolute deviation around the median, *J. Exp. Soc. Psychol.*, **49**, 764–766.
- Lyons, J.J., Waite, G.P., Ichihara, M. & Lees, J.M., 2012. Tilt prior to explosions and the effect of topography on ultra-long-period seismic records at Fuego volcano, Guatemala, *Geophys. Res. Lett.*, **39**, doi:10.1029/2012GL051184.
- Mader, H.M., Phillips, J.C. & Sparks, R.S.J., 1996. Dynamic of explosive degassing of magma: observations of fragmenting two-phase flows, *J. geophys. Res.*, **101**(B3), 5547–5560.
- Matoza, R.S. & Fee, D., 2014. Infrasonic component of volcano-seismic eruption tremor, *Geophys. Res. Lett.*, **41**, 1964–1970.
- Molina, I., Viracucha, G., Cobacango, P., Palacios, P., Mothes, P., Ruiz, A.G., Barba, D. & Arellano, S., 2006. *Resumen mensual, actividad del volcán Tungurahua, julio 2006*, Tech. Rep., Escuela Politécnica Nacional, Departamento de Geofísica.
- Mora, M.M., Lesage, P., Dorel, J., Bard, P.Y., Metaxian, J.P., Alvarado, G.E. & Leandro, C., 2001. Study of seismic site effects using H/V spectral ratios at Arenal volcano, Costa Rica, *Geophys. Res. Lett.*, **28**(15), 2991–2994.
- Nakamura, Y., 1989. A method for dynamic characteristics estimation of subsurface using microtremor on the ground surface, *Tech. Rep.*, **30**(1), Railway Technical Research Institute.
- Nakano, M. & Kumagai, H., 2005. Waveform inversion of volcano-seismic signals assuming possible source geometries, *Geophys. Res. Lett.*, **32**, L12302, doi:10.1029/2005GL022666.
- Nardone, L. & Maresca, R., 2011. Shallow velocity structure and site effects at Mt. Vesuvius, Italy, from HVSR and array measurements of ambient vibrations, *Bull. seism. Soc. Am.*, **101**(4), 1465–1477.
- Nishimura, T. & Chouet, B., 2003. A numerical simulation of magma motion, crustal deformation, and seismic radiation associated with volcanic eruptions, *Geophys. J. Int.*, **153**, 699–718.
- Nishimura, T., Iguchi, M., Kawaguchi, R., Hendrasato, M. & Rosadi, U., 2012. Inflatons prior to Vulcanian eruptions and gas burst detected by tilt observations at Semeru Volcano, Indonesia, *Bull. Volcanol.*, **74**, 903–911.

- Peterson, J., 1993. Observations and modeling of seismic background noise, U.S. Geological Survey, Open-File Report 93-322.
- Prieto, G.A., Denolle, M., Lawrence, J.F. & Beroza, G.C., 2011. On amplitude information carried by the ambient seismic field, *C. R. Geosci.*, **343**, 600–614.
- R Core Team, 2014. R: A language and environment for statistical computing, R Foundation for Statistical Computing, Vienna, Austria, <http://www.R-project.org/>.
- Ritzwoller, M.H., Lin, F.C. & Shen, W., 2011. Ambient noise tomography with a large seismic array, *C. R. Geosci.*, **343**, 558–570.
- Rowe, C.A., Aster, R.C., Kyle, R.P. & Dibble R.R. & Schlue, J.W., 2000. Seismic and acoustic observations at Mount Erebus Volcano, Ross Island, Antarctica, 1994–1998, *J. Volc. Geotherm. Res.*, **101**, 105–128.
- Sato, H., Fehler, M.C. & Maeda, T., 2012. *Seismic Wave Propagation and Scattering in Heterogeneous Earth*, 2nd edn, Springer.
- Sciotto, M., Cannata, A., Di Gracia, G., Gresta, S., Privitera, E. & Spina, L., 2011. Seismoacoustic investigations of paroxysmal activity at Mt. Etna volcano: new insights into 16 November 2006 eruption, *J. geophys. Res.*, **116**, doi:10.1029/2010JB008138.
- Shapiro, N.M., Campillo, M., Stehly, L. & Ritzwoller, M.H., 2005. High-resolution surface-wave tomography from ambient seismic noise, *Science*, **307**, 1615–1618.
- Shumway, H. & Stoffer, D., 2010. *Time Series Analysis and Its Applications*, 3rd edn, Springer.
- Takemura, S., Furumura, T. & Saito, T., 2009. Distortion of the apparent S-wave radiation pattern in the high-frequency wavefield: Tottori-Ken Seibu, Japan, *Geophys. J. Int.*, **178**, 950–961.
- Ward, K.M., Porter, R.C., Zandt, G., Beck, S.L., Wagner, L.S., Minaya, E. & Tavera, H., 2013. Ambient noise tomography across the Central Andes, *Geophys. J. Int.*, **194**, 1559–1573.
- Wegler, U. & Sens-Schönfelder, C., 2007. Fault zone monitoring with passive image interferometry, *Geophys. J. Int.*, **168**, 1029–1033.

APPENDIX: NOISE AND EXPLOSION DATA

Seismic noise traces.

| BRUN | BCUS, BMAS1 |
|----------------------|----------------------|
| 20140112 06:00–06:59 | 20060719 01:00–01:19 |
| 20140112 07:00–07:59 | 20060719 01:21–01:59 |
| 20140112 08:00–08:59 | 20060720 01:20–01:59 |
| 20140112 09:00–09:59 | 20060720 02:20–02:40 |
| 20140113 07:00–07:59 | 20060720 16:00–16:59 |
| 20140113 08:00–08:59 | 20060720 17:00–17:17 |
| 20140114 03:00–03:59 | 20060720 17:19–17:39 |
| 20140114 07:00–07:59 | 20060721 12:00–12:59 |
| 20140114 08:00–08:59 | 20060721 13:20–13:59 |
| 20140115 04:00–04:59 | 20060721 14:00–14:20 |
| 20140115 05:00–05:59 | 20060724 23:10–23:40 |
| 20140115 07:00–07:59 | |
| 20140115 08:00–08:59 | |
| 20140116 04:00–04:59 | |
| 20140120 06:00–06:59 | |
| 20140120 07:00–07:59 | |
| 20140121 08:00–08:59 | |
| 20140123 08:00–08:59 | |
| 20140124 04:00–04:59 | |
| 20140124 05:00–05:59 | |

Explosions.

| | |
|----------------|----------------|
| 20060720 05:22 | 20060721 02:45 |
| 20060720 05:47 | 20060721 04:04 |
| 20060720 07:29 | 20060721 05:11 |
| 20060720 08:10 | 20060721 05:46 |
| 20060720 08:58 | 20060721 08:07 |
| 20060720 12:53 | 20060721 09:30 |
| 20060720 19:21 | 20060721 10:27 |
| 20060720 22:38 | 20060721 10:54 |
| 20060720 23:07 | 20060721 19:00 |
| 20060721 02:24 | 20060721 19:04 |